King Saud University

Arabian Journal of Chemistry

www.ksu.edu.sa
www.sciencedirect.com

ORIGINAL ARTICLE

Fabrication of inorganic alumina particles at nanoscale by a pulsed laser ablation technique in liquid and exploring their protein binding, anticancer and antipathogenic activities

Amir Jouya Talaei [a,b,1], **Nahid Zarei** [c,1], **Anwarul Hasan** [d,e], **Samir Haj Bloukh** [f], **Zehra Edis** [g], **Niusha Abbasi Gamasaee** [h], **Marjan Heidarzadeh** [i], **Mohammad Mahdi Nejadi Babadaei** [j], **Koorosh Shahpasand** [k], **Majid Sharifi** [l], **Keivan Akhatri** [m], **Suliman Khan** [a,*], **Menzghou Xue** [a,*], **Mojtaba Falahati** [l,*]

[a] *Department of Cerebrovascular Diseases, The Second Affiliated Hospital of Zhengzhou University, Zhengzhou, PR China*
[b] *Department of Biotechnology, Faculty of Basic Science, East Tehran Branch, Islamic Azad University, Tehran, Iran*
[c] *Department of Cellular and Molecular Biology, Faculty of Advanced Sciences and Technology, Tehran Medical Sciences, Islamic Azad University, Tehran, Iran*
[d] *Department of Mechanical and Industrial Engineering, College of Engineering, Qatar University, Doha 2713, Qatar*
[e] *Biomedical Research Center, Qatar University, Doha 2713, Qatar*
[f] *Department of Clinical Sciences, College of Pharmacy and Health Sciences, Ajman University, PO Box 346 Ajman, United Arab Emirates*
[g] *Department of Pharmaceutical Sciences, College of Pharmacy and Health Sciences, Ajman University, PO Box 346 Ajman, United Arab Emirates*
[h] *Department of Genetics, Faculty of Advanced Sciences and Technology, Tehran Medical Sciences, Islamic Azad University, Tehran, Iran*
[i] *Department of Food Toxicology, Research Center of Food Technology and Agricultural Products, Standard Research Institute (SRI), Karaj, Iran*
[j] *Department of Molecular Genetics, Faculty of Biological Science, North Tehran Branch, Islamic Azad University, Tehran, Iran*
[k] *Department of Stem Cells and Developmental Biology, Cell Science Research Center, Royan Institute for Stem Cell Biology and Technology (RI-SCBT), Tehran, Iran*
[l] *Department of Nanotechnology, Faculty of Advanced Sciences and Technology, Tehran Medical Sciences, Islamic Azad University, Tehran, Iran*
[m] *Department of Physics, University of Kurdistan, Sanandaj, Iran*

* Corresponding authors.
 E-mail addresses: suliman.khan18@mails.ucas.ac.cn (S. Khan), xuemengzhou@zzu.edu.cn (M. Xue), mojtaba.falahati@alumni.ut.ac.ir (M. Falahati).
 [1] These authors are joint first authors and contributed equally to this work.

ELSEVIER **Production and hosting by Elsevier**

Abstract The interaction of nanoparticles with biological systems can provide useful information about their therapeutic applications. The aluminum nanoparticles (Al_2O_3 NPs) were synthesized by laser ablation technique and well-characterized by different methods. Fluorescence spectroscopy, circular dichroism (CD) spectroscopy, and molecular docking studies were employed to evaluate the effect of Al_2O_3 NPs on the protein structure. Growth inhibitory and apoptotic effects of the Al_2O_3 NPs against K562 cancer cells and lymphocyte cells were assessed using [3-(4,5-dimethylthia zol-2-yl)-2,5-diphenyltetrazolium bromide] (MTT), flow cytometry, and real time polymerase chain reaction (PCR) assays. The antipathogenic activity of Al_2O_3 NPs against a diverse range of Gram-negative and Gram-positive pathogens was explored through a disk diffusion method. The characterization techniques determined that the Al_2O_3 NPs were successfully synthesized in the nanoscales. Intrinsic, 1-anilino-8-naphthalenesulfonate (ANS) and acrylamide fluorescence spectroscopy studies disclosed that Al_2O_3 NPs can partially change the tertiary structure of human serum albumin (HSA), whereas CD spectroscopy investigation depicted that the secondary structure of HSA remained intact. Molecular docking investigation also manifest that the Al_2O_3 nano-clusters preferably bind to electrostatic residues. Al_2O_3 NPs exhibited promising and selective anticancer features through reactive oxygen species (ROS) production, apoptosis induction, and elevation of Bax/Bcl-2 mRNA ratio. Furthermore, the Al_2O_3 NP showed a remarkable antibacterial activity against both Gram-negative and Gram-positive pathogens. In conclusion, it may be suggested that the synthesized Al_2O_3 NPs can be integrated in the development of anticancer and antipathogenic agents.

1. Introduction

Nanotechnology is the control of materials in a nanosized range, giving rise to unique physical, chemical, and biological activities, enabling new and unique applications (Ariga et al., 2015). Therefore, NPs are extensively utilized in the development and improvement of the quality of many biological and pharmaceutical products (Nikalje, 2015).

Nowadays, cancer is one of the leading causes of death worldwide (Bray et al., 2018). Many current therapeutic approaches for cancer therapy have failed to influence disease progression. Hence, the advancement of potential technologies in the prevention and treatment of cancer can be promising. The application of NPs in therapeutic activities has the great potential to change the future of cancer therapy (Hartshorn et al., 2017, Jurj et al., 2017, Sharifi et al., 2019a, Sharifi et al., 2019b). NPs can be engineered to selectively target a cancer cell and potentially accumulate within the tumor microenvironment (He et al., 2018, Sharifi et al., 2019a). The use of NPs as drug adjuvants or drug delivery vehicles results in a greater amount of drug loading at the tumor site and thus improving the efficiency of cancer therapy and reduces the harmful and uncertain side effects of conventional strategies (Huang et al., 2018, Yang et al., 2018).

In other ways, almost a number of microorganisms are inherently capable of resisting many therapeutic approaches because of the ease of genetic mutation (Van Duijkeren et al., 2018). Pharmaceutical companies are losing interest in developing new antibiotics and changing investment and research in more profitable areas. Clever solutions are needed to overcome these concerns and to combine affordable, low-cost, and high efficiency manufacturing processes. In this context, NP-based platforms are considered as promising strategies for development of potential antibacterial agents (Muzammil et al., 2018, Ramos et al., 2018).

Alumina (Al_2O_3) NPs have shown a wide range of applications in different fields such as photocatalytic platforms (Areerachakul et al., 2019), piezoelectric devices (Kumar et al., 2019), pigments (Liang et al., 2019), chemical sensors (Fu et al., 2019), drug carriers (Usman et al., 2020), and development of antipathogenic systems (Dabagh et al., 2018).

In the last few decades, synthesis of different NPs by pulsed laser ablation method in liquid phase has attracted the attention of many researchers (Zeng et al., 2012, Shankar et al., 2020, Mintcheva et al., 2020). Indeed, in comparison with other methods, typically chemical approaches, laser ablation in liquid provides a simple and green platform that usually works in different liquids (Zeng et al., 2012). It has been reported that the synthesis of Al_2O_3 NPs can be done through pulsed Nd–YAG laser to produce without any surfactants or catalysts (Lee et al., 2012). Also, it has been reported that the fabricated Al_2O_3 NPs by pulsed laser ablation in liquid show potential thermal conductivity (Riahi et al., 2020) with novel wettability and nonlinearity properties (Iqbal et al., 2020).

However, despite the widespread and pharmaceutical application of NPs-based products, there is still no clear and definitive knowledge and understanding of the effects of these NPs on biomacromolecules and biological systems. Importantly, the lack

of a standard NP assay and a detailed description of the molecular mechanism of their activity have resulted in production of conflicting outcomes. Therefore, evaluating the protein binding properties of NPs and corresponding conformational changes of proteins is a major concern for using NPs in medical applications (Anbouhi et al., 2019, Behzadi et al., 2019; Falahati et al., 2019b; Roudbaneh et al., 2019). Because, NPs are surrounded by proteins (protein corona) as they enter the cell microenvironment, the amount and mode of binding of proteins to NPs depend on the physicochemical properties of the NPs induced by the synthesis routes selected (Falahati et al., 2019a). The protein interaction between NPs and proteins can be dynamic or static and different degrees of protein structural alterations have been reported upon adsorption of proteins on the NP surface (Aghili et al., 2016, Esfandfar et al., 2016, Hajsalimi et al., 2018, Sharifi et al., 2019c).

Human serum albumin (HSA) is the most abundant protein in plasma with various physiological and pharmacological functions. This protein plays an important role in the transport and distribution of drugs in the blood (Esfandfar et al., 2016). Since NPs are capable of binding HSA, it is important to study the interaction of NPs with HSA by biophysical techniques (Anbouhi et al., 2019, Falahati et al., 2019b, Roudbaneh et al., 2019). Generally, when a NP is introduced as an anti-cancer or antibacterial agent, along with its medicinal features, its protein binding properties should be also analyzed. Hence, in this paper, the interaction of Al_2O_3 NPs with HSA, K562 cells, lymphocyte cells, Gram-positive, and Gram-negative bacteria was explored by their respective assays.

2. Materials and methods

2.1. Materials

HSA, MTT, Al_2O_3 powder, and ANS were purchased from Sigma-Aldrich Co. (Sigma-Aldrich, USA). Roswell Park Memorial Institute (RPMI-1640) and fetal bovine serum (FBS) were obtained from Gibco Co. (Dublin, Ireland).

2.2. Synthesis of Al_2O_3 NPs

The laser ablation technique was used to fabricate Al_2O_3 NPs based on the Piriyawong et al. (2012) study. Briefly, Al_2O_3 powder was turned into a pellet by pressure (100 bars), followed by placing at the bottom of a vessel. Then, 10 mL of deionized water (DW) was added to the vessel until its level was 5 mm above the sample. The 1064 nm Nd:YAG laser with an energy of 3 J, a repetition rate of 2 Hz, a focus of 50 mm focal-length lens, and laser ablation energy of 5,000 pulses for the total time of about 30 min. Afterward, the Al_2O_3 NPs dispersed in DW was obtained.

2.3. Characterization of synthesized Al_2O_3 NPs

Synthesized NPs were solubilized in ethanol and sonicated for 20 min at room temperature. Afterwards, the samples were dried and the micrograph was obtained using a Zeiss transmission electron microscopy (TEM, EM10C, 100 KV, Germany). The hydrodynamic radius and zeta potential value of fabricated Al_2O_3 NPs were determined using dynamic light scattering (DLS) technique by a Brookhaven instruments 90Plus particle size /zeta analyzer (Holtsville, NY, USA). The crystalline state of synthesized Al_2O_3 NPs was determined using X-ray diffraction (XRD) analysis. The experiment was done using a Philips diffractometer XRD PW 1730 CuKα, scanning speed of 0.05°/min, and in $2\theta = 5\text{-}80°$ range.

2.4. Preparation of HSA solution and Al_2O_3 NP dispersions

Both protein powder and Al_2O_3 nano-powder were solubilized in a phosphate buffer (20 mM, pH 7.5). Furthermore, Al_2O_3 NP colloidal solution was sonicated for 2 min at room temperature. Protein concentration determination was done based on the Beer-Lambert law, where the molar extinction coefficient of HSA was 35700 M^{-1} cm^{-1}.

2.5. Intrinsic fluorescence spectroscopy study

Intrinsic fluorescence spectroscopy was done to investigate the structural changes of HSA (0.1 mg/ml) after interaction with varying concentrations (0.05–50 μg/ml) of Al_2O_3 NPs using a Cary Eclipse fluorescence spectrofluorometer (Varian, Australia).

In this experiment, the excitation signals were set at 295 nm (slit width of 10 nm), where emission signals were read between 300 and 450 nm (slit width of 10 nm).

2.6. ANS fluorescence study

ANS fluorescence spectroscopy was carried out to explore the 3D structural changes of HSA upon incubation with varying concentrations (0.05–50 μg/ml) of Al_2O_3 NPs. A protein solution with fixed concentrations of HSA (0.1 mg/ml) and ANS (15 μM) was tittered by varying concentrations of Al_2O_3 NPs (0.05–50 μg/ml) and excitation signal was fixed at 380 nm with slit width of 10 nm, where emission signal was read between 400 and 600 nm with slit width of 10 nm.

2.7. Acrylamide quenching study

The intrinsic fluorescence intensity of the HSA either alone or with different concentrations (0.05–50 μg/ml) of Al_2O_3 NPs were measured in the presence of varying concentrations of acrylamide (0–0.5 M) at room temperature. The λ_{max} of each sample was measured and reported as F_0 (fluorescence intensity in the absence of NPs) or F (the fluorescence intensity in the presence of different concentrations of NPs). The resulting data were analyzed with a Stern-Volmer Eq. as following:

$$F_o/F = K_{SV}[\text{Acrylamide}] + 1 \tag{1}$$

where, K_{SV} determines the Stern-Volmer constant.

2.8. Molecular docking study

The molecular docking analysis was performed to investigate the interaction of HSA molecules with Al_2O_3 nano-clusters using Hex 6.3 software (http://hexserver.loria.fr/). Five nano-clusters of Al_2O_3 particles with varying dimensions and morphologies were used as different models of the Al_2O_3 NPs.

The 3D structure of HSA (PDB number: 1AO6) was downloaded from the protein data bank. The water molecules were removed from the HSA structure and the crystal conformations were checked and all probable missing atoms were corrected. The sites involved in the interaction of HSA with various Al_2O_3 nano-clusters were given scores based on an E-value.

2.9. Circular dichroism study

The far-UV CD bands (190 to 260 nm) of HSA (0.5 mg/ml) were detected in the presence of varying concentrations of Al_2O_3 NPs (0.05–50 µg/ml) using spectropolarimeter (model 215, Aviv, Lakewood, NJ, USA). The secondary structural alterations of HSA in the presence of Al_2O_3 NPs were then estimated using CDNN software.

2.10. Cell culture

The human leukemia cell line (K562) was obtained from the Pasteur Institute (Tehran, Iran). Human peripheral lymphocytes were extracted by gradient centrifugation on Ficoll-Paque PLUS (Sigma, USA) based on Ethics were approved by the Ethics Committee of the Azad University. The cells were cultured in RPMI-1640 medium supplemented with FBS (1 0 5), streptomycin (100 µg/ml) and penicillin (100 U/ ml) at 37 °C in a 5% CO_2 humidified atmosphere.

2.11. MTT assay

To investigate the Al_2O_3 NPs-induced mortality on K562 and lymphocyte cells, the cells were exposed to varying various concentrations of Al_2O_3 NPs (0.05–50 µg/mL) for 24 hrs. Afterwards, the percentage of viable cells was explored by MTT assay at 570 nm employing an ELISA reader (Expert 96, Asys Hitch, Ec Austria).

2.12. ROS assay

The Al_2O_3 NPs-stimulated generation of intracellular ROS was examined using DCFDA/ H_2DCFDA - Cellular ROS Assay Kit (ab113851). Briefly, following treatments of K562 cells with highest concentration (50 µg/ml) of Al_2O_3 NPs, the cells were collected and stained with 30 µM of DCFH-DA for 40 min. The fluorescence intensity of the cells was examined employing flow cytometry (FACSCalibur; BD Biosciences, San Jose, CA, USA) and FlowJo software.

2.13. Apoptosis assay

Annexin V-FITC Apoptosis Staining/Detection Kit (ab14085) was used to calculate the degree of apoptosis and necrosis triggered by Al_2O_3 NP against K562 cells. Briefly, after treatment of cells with highest concentration (50 µg/ml) of Al_2O_3 NPs, cells were collected, re-suspended in 500 µl of 1X Annexin V binding buffer, and stained with 5 µl of Annexin V-FITC and 5 µl propidium iodide (PI). The percentage of apoptotic and necrotic cells was then calculated through flow cytometry (FACSCalibur; BD Biosciences, San Jose, CA, USA) and FlowJo software.

2.14. Quantitative real time PCR (qPCR) analysis

The Al_2O_3 NP-induced expression of B-cell lymphoma-2 (Bcl-2) and Bax mRNA was analyzed using qPCR assay. TRIzol reagent was employed to extract total RNA based on the manufacturer's protocols (Thermo Fisher Scientific, Waltham, MA, USA). The synthesis of cDNA was done according to the manufacturer's instructions (RevertAid first-strand cDNA synthesis kit, Takara, Japan). The primer sequences for GAPDH, Bax and Bcl-2 mRNA were, Fw: ACACCCACT CCTCCACCTTTG, Rev: TCCACCACCCTGTTGCTG-TAG; Fw: GGGTGGTTGGG TGAGACTC, Rev: AGA-CACGTAAGGAAAACGCATTA; Fw: AACGTGCCTC ATGAAATAAAG, Rev:TTATTGGATGTGCTTTGCAT TC, respectively.

qPCR was then done using an ABI Step One Sequence Detection System (Thermo Fisher Scientific) with SYBR® Premix Taq™ II (Takara, Japan). The relative expression levels of Bcl-2 and Bax were calculated relative to GAPDH as a control gene. Comparative threshold cycle ($2^{-\Delta\Delta CT}$) method was used to express the outcome.

2.15. Agar well diffusion method

Agar well diffusion method was used to assess the antipathogenic activity of Al_2O_3 NP against several pathogenic bacteria including Escherichia coli (ATCC 25922), Pseudomonas aeruginosa (ATCC 27853) and Staphylococcus aureus (ATCC 25923). These strains were cultured in LB broth and were covered over the agar plate using sterile cotton swabs. The 8 mm diameter well was punched on nutrient agar and different concentrations of Al_2O_3 NPs (200–1.6 µg/mL) was added to each well and incubated for 24 hrs at 37 °C.

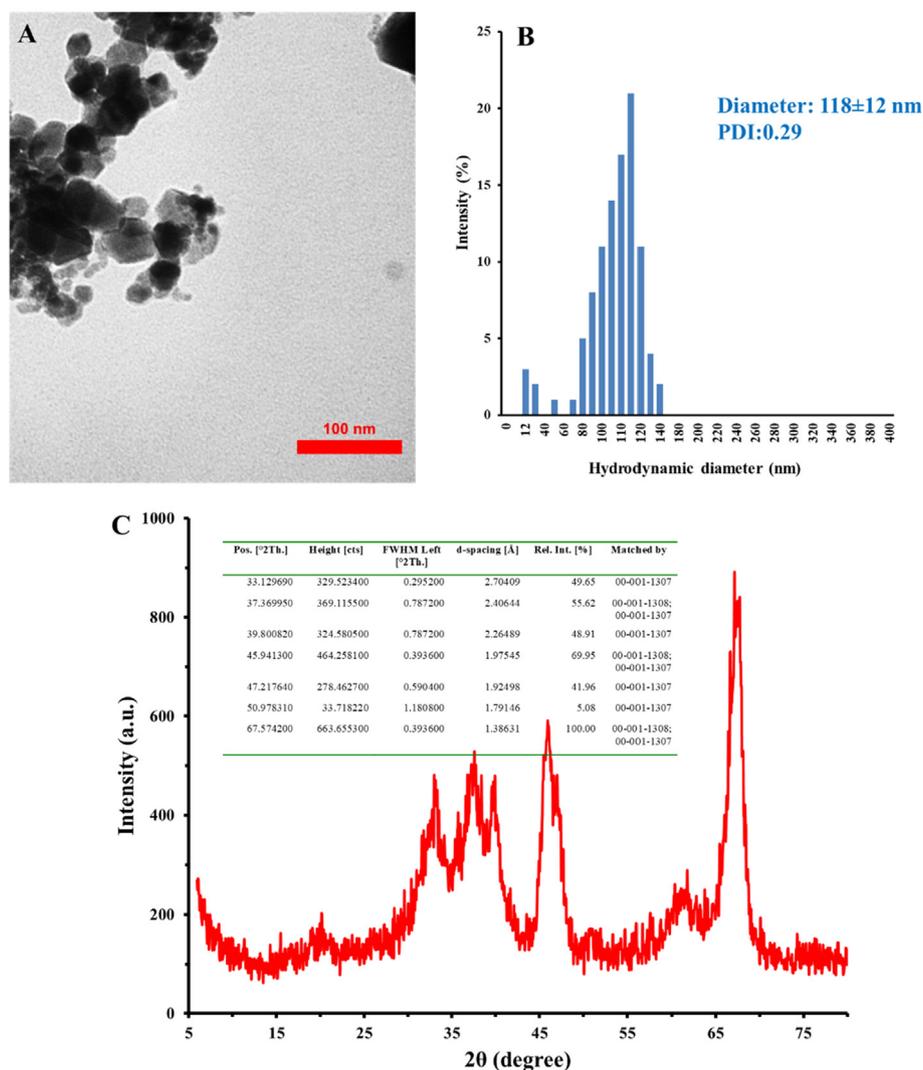## 2.16. Statistical analyses

One-way analysis of variance (ANOVA) was performed by using Statistical Package for Social Science (version 20; SPSS Inc, Chicago, IL) followed by Dunnett's multiple comparison tests and are displayed as means ± SDs. $P < 0.05$ was exhibited statistically significant.

3. Results

3.1. Al_2O_3 NPs characterization

Laser ablation which is known as a simple approach for synthesizing the metal NPs without chemical compounds or surfactant was used as a feasible, safe and cost-effective method for fabrication of Al_2O_3 NPs. Information on the characteristic dimension of the Al_2O_3 NPs fabricated by laser ablation technique was obtained by TEM analysis. TEM image of Al_2O_3 NPs is depicted in Fig. 1A. TEM image exhibits slightly aggregated form of synthesized NPs with similar geometries, rounded edges and a size range from 20 nm to 60 nm. DLS study was done to measure the hydrodynamic diameter and zeta potential value of synthesized Al_2O_3 NPs. Fig. 1B shows that the hydrodynamic diameter of Al_2O_3 NPs was around 118 ± 12 nm with a PDI of 0.29. Moreover, zeta potential value was determined to be −31.81 mV, indicating a good col-

Pos. [°2Th.]	Height [cts]	FWHM Left [°2Th.]	d-spacing [Å]	Rel. Int. [%]	Matched by
33.129690	329.523400	0.295200	2.70409	49.65	00-001-1307
37.369950	369.115500	0.787200	2.40644	55.62	00-001-1308; 00-001-1307
39.800820	324.580500	0.787200	2.26489	48.91	00-001-1307
45.941300	464.258100	0.393600	1.97545	69.95	00-001-1308; 00-001-1307
47.217640	278.462700	0.590400	1.92498	41.96	00-001-1307
50.978310	33.718220	1.180800	1.79146	5.08	00-001-1307
67.574200	663.655300	0.393600	1.38631	100.00	00-001-1308; 00-001-1307

Fig. 1 TEM image (A), DLS histogram (B), and XRD pattern (C) of synthesized Al_2O_3 NPs. The inset shows the XRD data.

loidal stability of synthesized Al_2O_3 NPs. Fig. 1C also displays the XRD pattern of synthesized Al_2O_3 NPs. It was determined that crystalline structure of Al_2O_3 NPs depicts 7 characteristics peaks presented at 33.12°, 37.36°, 39.80°, 45.94°, 47.21°, 50.97°, and 67.57° with real intensities of 49.65%, 55.62%, 48.91%, 69.95%, 41.96%, 5.08%, and 100%, respectively (Fig. 1C, inset), corresponding to crystalline structure of γ-Al_2O_3 NPs reported by Piriyawong et al. (2012).

3.2. Fluorescence spectroscopy studies:

Protein molecules are documented to show intrinsic fluorescence intensity mostly deriving from the aromatic residues (Zeinabad et al., 2016, Sabziparvar et al., 2018). When proteins interact with small molecules, their intrinsic fluorescence intensity almost alters with the small molecule's concentration. Subsequently, changes in the fluorescence intensity of receptors can be considered as an important probe for studying the conformational changes of protein after interaction with ligands (Zeinabad et al., 2016).

In this assay, the concentration of HSA solutions was fixed and different concentrations (0.05, 1, 10, 20, and 50 µg/ml) of Al_2O_3 NPs were added to the protein solution. Fluorescence intensity of HSA after the addition of different concentrations of Al_2O_3 NPs was read upon excitation at 295 nm at room temperature, as exhibited in Fig. 2A. It was displayed that HSA showed a strong fluorescence intensity at 342 nm. However, the fluorescence signals of HSA decreased continually with enhancing the concentration of Al_2O_3 NPs, which determines that the aromatic residues of HSA are partially displaced to a more hydrophilic microenvironment after the interaction with Al_2O_3 NPs.

To more examine the microenvironmental alterations of hydrophobic moieties of HSA upon interaction with different concentrations of Al_2O_3 NPs, the structural changes of HSA were probed by detecting ANS fluorescence signals of the protein. It was observed that free HSA shows a relatively weak ANS fluorescence intensity, indicating the folded state of protein in the absence of Al_2O_3 NPs (Fig. 2B). However, it was exhibited that after addition of varying concentrations (0.05,
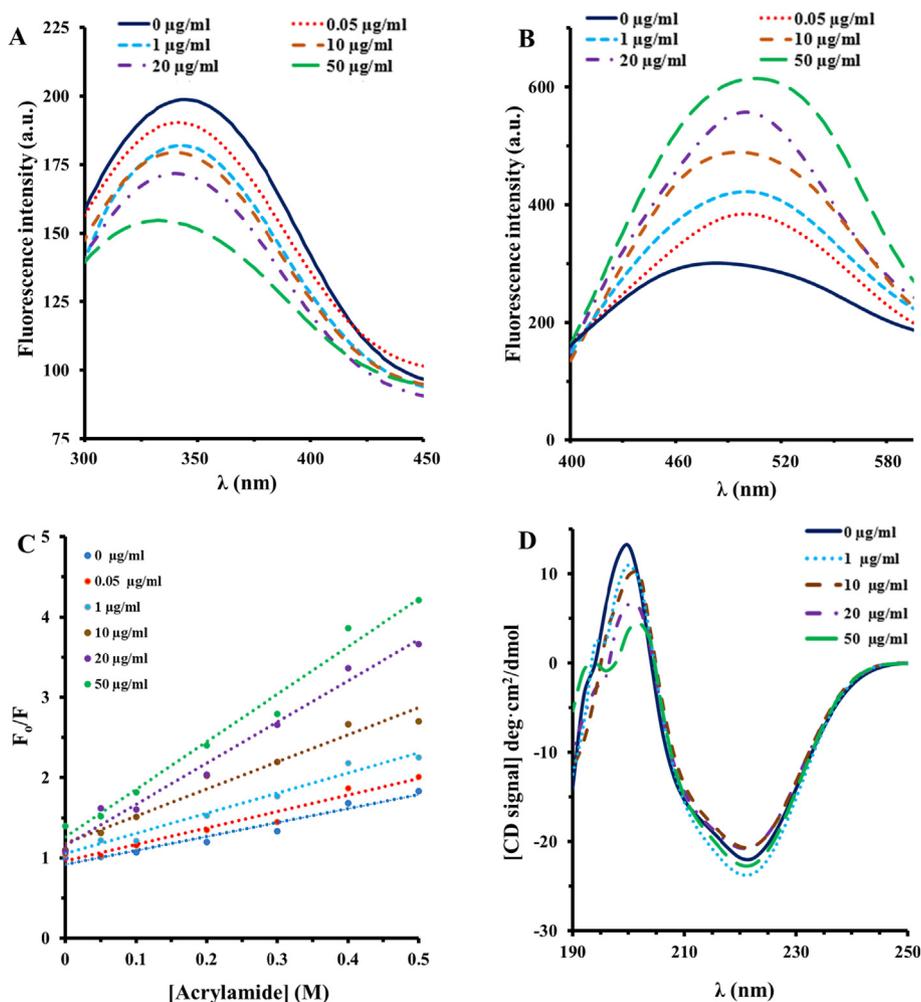
Fig. 2 Fluorescence quenching (A), ANS fluorescence (B), Stern-Volmer plot of acrylamide quenching (C), and CD spectra (D) of HSA in thepresence of varying concentrations of Al_2O_3 NPs at room temperature.

Table 1 K_{SV} values of HSA quenching induced by acrylamide in the presence of varying concentrations of Al_2O_3 NPs.

[Al_2O_3 NPs] (µg/ml)	K_{SV} (M^{-1})	R^2
0	1.73	0.98
0.05	2.05	0.97
1	2.50	0.96
10	3.36	0.95
20	5.13	0.96
50	5.92	0.95

1, 10, 20, and 50 µg/ml) of Al_2O_3 NPs, a substantial increase in the ANS fluorescence spectrum of HSA was detected in a concentration-dependent manner, corresponding to conformational changes of HSA molecules in the presence of Al_2O_3 NPs. Therefore, intrinsic and ANS fluorescence outcomes revealed that different concentrations of Al_2O_3 NPs increased the NP-stimulated conformational alterations of HSA.

The investigation of fluorescence quenching of HSA induced by acrylamide was also done to analyze the conformational changes of HSA in the presence of different concentrations (0.05, 1, 10, 20, and 50 µg/ml) of Al_2O_3 NPs (Falahati

et al., 2012). Indeed, fluorescence quenching of HSA either alone or with different concentrations of Al_2O_3 NPs disclose their interaction with acrylamide. The fluorescence quenching of HSA induced by acrylamide were analyzed by using the Stern–Volmer equation (Fig. 2C) and the calculated K_{SV} in the presence of different concentrations (0.05, 1, 10, 20, and 50 µg/ml) of Al_2O_3 NPs are shown in Table 1. As demonstrated in Fig. 2C and summarized in Table 1, the K_{SV} values of HSA-acrylamide species enhance with increasing concentrations of Al_2O_3 NPs, revealing that the probable Al_2O_3 NPs-induced structural changes of HSA. Generally, these outcomes suggested that the accessibility of aromatic residues in HSA molecules to acrylamide is higher in the presence of Al_2O_3 NPs relative to the absence of NPs.

3.3. CD spectroscopy study

CD spectroscopy is considered as an outstanding technique for detecting the secondary structural alterations in biomolecules induced by NPs (Mansouri et al., 2018, Gilan et al., 2019). The far- UV CD signals of HSA molecules either alone or in the presence of different concentrations (1, 10, 20, and 50 µg/ml) of Al_2O_3 NPs are depicted in Fig. 2D. It was

revealed that the CD spectrum of protein shows 2 minima at 222 and 208 nm, revealing that α-helix is the most predominant secondary structure in HSA. The comparison of far-UV CD signals of HSA in the presence of different concentrations of Al_2O_3 NPs revealed that NPs in any applied concentrations did not induce a remarkable change in the observed ellipticity values of HSA molecules. This data may indicate that the secondary structure of HSA remained intact in the presence of varying concentrations of Al_2O_3 NPs.

3.4. Molecular docking study

The molecular docking analysis was run to evaluate the binding energies and residues involved in the interaction of different Al_2O_3 nano-clusters with HSA [20, 25]. Using Hex 6.3 software, 5 different Al_2O_3 nano-clusters were docked onto binding sites of HSA molecules (Fig. 3A–E). The Al_2O_3 nano-clusters displayed an exothermic binding process with different binding scores ranging between −391.40 and − 717.45 E-value. The best scoring was for the cubic Al_2O_3 nano-clusters with a diameter of 2 nm and a binding energy of − 717.45 E-value (Table 2). Fig. 3A–E demonstrates the binding affinity of different Al_2O_3 nano-clusters on different sites of HSA. Cubic nano-cluster provides the highest binding affinity for HSA, followed by spherical nano-cluster (r = 1.5 nm), spherical nano-cluster (r = 0.5 nm), conical nano-cluster (r = 1 nm, h = 1.5 nm), and spherical nano-cluster (r = 1 nm). Visualization of amino acid residues of docked complexes was performed via the PyMOL tool (https://pymol.org) (Fig. 4A–E). Thus, it was shown that HSA is able to bind many different types of Al_2O_3 nano-clusters through different amino acid residues depending on the physicochemical properties of nano-clusters.

Thus, different binding sites are localized for Al_2O_3 nano-clusters in the HSA subdomains. Cubical nano-clusters (a = 2 nm) preferably binds to the electrostatic sites in HSA subdomain which is surrounded by charged amino acids residues such as Asp-187, Asp-183, Lys-439, Glu-396, Glu-400, Lys-402, Arg-521, Lys-519, and Glu-518. Also, some hydrophilic and very small portions of hydrophobic residues were recognized in the binding site. In general, analysis of interaction and recognition of the amino acid residues involved in interaction of different types of Al_2O_3 nano-clusters and HSA exhibited that Al_2O_3 nano-clusters preferably bind to the amino acid residues at each binding site by electrostatic forces (Table 2).

These outcomes are consistent with the intrinsic fluorescence spectroscopic analysis and provide further evidence for fluorescence quenching of HSA by Al_2O_3 NPs.

3.5. MTT assay

The anticancer and the cytotoxic effects of Al_2O_3 NPs against K562 and lymphocytes were done by MTT assay. As displayed in Fig. 5, Al_2O_3 NPs reduced the proliferation of K562 cells in a dose-dependent manner. Indeed, after incubation of K562
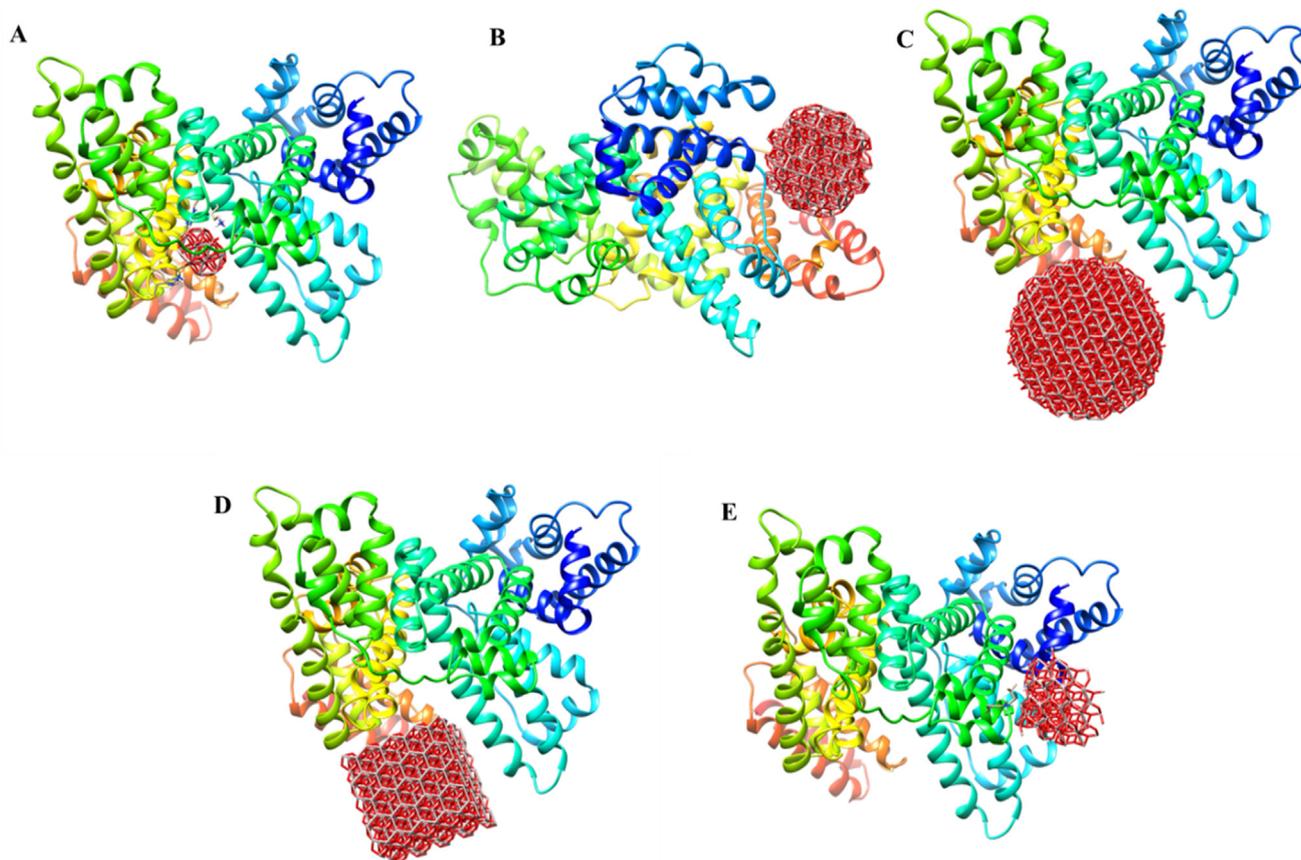
Fig. 3 HEX 6.3 results of the interaction of HSA with Al_2O_3 nano-clusters, spherical-shaped with r = 0.5 nm (A), spherical-shaped with r = 1 nm (B), spherical-shaped with r = 1.5 nm (C), cubical-shaped with a = 2 nm (D), conical-shaped with r = 1 nm, h = 1.5 nm (E).

Table 2 Docking results of Al$_2$O$_3$ nano-clusters with HSA molecules.

| Nano-cluster shape	Dimensions	Docking score (E-value)	Residue interacted
Sphere	r = 0.5 nm	−420.37	His-440, Lys-436, Cys-437, Lys-444, Cys-448, Pro-447, Thr-452, Lys-195, Glu-292, Val-293, Arg-218
Sphere	r = 1 nm	−375.17	Glu-82, Thr-83, Gln-33, Arg-144, Asn-111, Pro-113, Tyr-140, Pro-35, Phe-36, Glu-36, Lys-137, Pro-113
Sphere	r = 1.5 nm	−678.09	Lys-560, Glu-518, Gln-522, Tyr-401, Lys-402, Glu-400, Gly-399, Leu-398, Glu-396, Lys-439, Phe-395, Ser-435
Cube	a = 2 nm	−717.45	Asp-187, Asp-183, Lys-439, Ser-435, Glu-396, Phe-395, Gln-397, Leu-398, Gly-399, Glu-400, Lys-402, Arg-521, Lys-519, Glu-518, Gln-522
Cone	r = 1 nm, h = 1.5 nm	−391.40	Asp-13, Leu-14, Asn-18, Ala-258, Lys-262, Leu-283, Pro-282, Glu-280, Cys-279, Lys-286

cells with different concentrations (0.05, 1,10,20, and 50 μg/ml) of Al$_2$O$_3$ NPs, the cell viability decreased to 91.35%, 83.23%, 74.45%, % 62.83, and 54.19% respectively. The cytotoxicity of Al$_2$O$_3$ NPs on lymphocyte cells was also explored by the MTT assay. It was observed that about 80.61% of the lymphocyte cells survived at the highest concentration (50 μg/ml) of Al$_2$O$_3$ NPs (Fig. 5). Therefore, it may be indicated that Al$_2$O$_3$ NPs can selectively suppress the proliferation of K562 cells.

3.6. ROS assay

It has been reported that elevation of intracellular ROS stimulated by NPs may be one of the most important active mechanisms in the anticancer effects of NPs. Therefore, in this study we aimed to reveal the level of ROS in control and treated k562 cells by flow cytometry. As displayed in Fig. 6A, control cells show a DCF intensity of 195 unit, whereas this amount increases to 750 unit after 24 hrs incubation of K562 cells with highest concentration (50 μg/ml) of Al$_2$O$_3$ NPs. It can be indicated that Al$_2$O$_3$ NPs stimulated a significant (***P < 0.001) increase in the ROS production in K562 cells after 24 hrs.

3.7. Apoptosis and necrosis assay

The rate of apoptosis stimulated by Al$_2$O$_3$ NPs in K562 cells was inspected by dual staining with Annexin V-FITC/PI assay, where the K562 cells incubated with highest concentration of
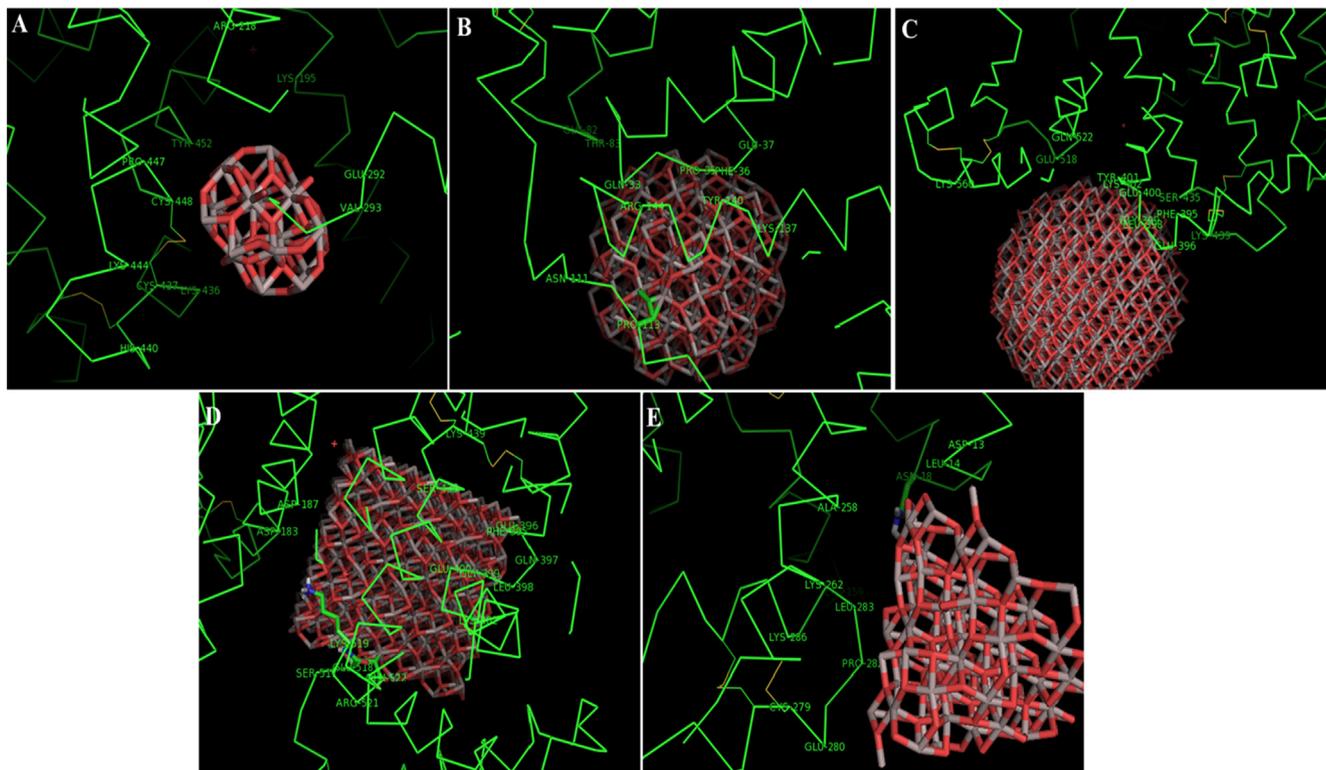
Fig. 4 Docking pose of HSA molecules upon interaction with Al$_2$O$_3$ nano-clusters spherical-shaped with r = 0.5 nm (A), spherical-shaped with r = 1 nm (B), spherical-shaped with r = 1.5 nm (C), cubical-shaped with a = 2 nm (D), conical-shaped with r = 1 nm, h = 1.5 nm (E).

Al_2O_3 NPs (50 µg/ml) for 24 hrs (Fig. 6B). Untreated negative control cells were demonstrated to be mostly viable, whereas the rate of early and late apoptosis and necrosis simultaneously enhanced in the presence of highest concentration of Al_2O_3 NPs. Actually, after 24 hrs exposure, a remarkable increase in rate of early apoptosis (***$P < 0.001$), late apoptosis (***$P < 0.001$), and necrosis (***$P < 0.001$) was detected in K562 cells incubated with highest concentration (50 µg/ml) of Al_2O_3 NPs (Fig. 6B).

3.8. qPCR analysis

Several factors such as Bcl-2 and Bax play a pivotal role in the execution of intrinsic apoptotic pathways. In order to explore the molecular mechanism by which Al_2O_3 NPs stimulate apoptosis in K562 cells, we assessed the expression levels of Bcl-2 mRNA and Bax mRNA using qPCR assay. We analyzed the expression pattern of Bcl-2 mRNA and Bax mRNA in K562 cells incubated with highest concentration (50 µg/ml) of Al_2O_3 NPs for 24 hrs. The outcome exhibited that Al_2O_3 NPs significantly (*$P < 0.5$) down-regulate the expression of Bcl-2 mRNA and concomitantly markedly (*$P < 0.5$) up-regulate the Bax mRNA expression after 24 hrs exposure (Fig. 6C).

3.9. Antibacterial activity by well diffusion method

The antibacterial activity of Al_2O_3NPs was evaluated against three strains of pathogens: *S. aureus*, *E. coli* and *P. aeruginosa*. The presence of a clear zone around the disks demonstrates that the Al_2O_3 NPs exhibited antipathogenic activity which is capable of limiting the growth of both Gram-negative and Gram-positive foodborne pathogens. As exhibited in Fig. 7, the Al_2O_3 NP displayed a remarkable anti-pathogenic activity against both Gram-negative and Gram-positive pathogens.

4. Discussion

In this paper, Al_2O_3 NPs were synthesized by laser ablation method and characterized by different techniques. It was shown that the particle size of the Al_2O_3 NPs with laser energy of 3 J were ranged from 20 to 60 nm, which is in good agreement with Piriyawong et al. (2012) study. It was determined that laser ablation method can transom Al salt into γ-Al_2O_3 which is also in good agreement with previously reported studies (Piriyawong et al., 2012, Lam et al., 2014, Kusper and Guisbiers, 2018). However, it should be emphasized that the laser fluence affect the characteristics of Al_2O_3 NPs synthesized by laser ablation in liquids (Abbasi et al., 2015, Ismail et al., 2017).

Since the HSA contains some active sites, it can be participated in ligand binding processes through van der Waals, hydrogen bonding, electrostatic interactions, and even hydrophobic forces (Chibber and Ahmad, 2016). In this study, based on multispectroscopic and theoretical analysis, we investigated the interactions of Al_2O_3 NPs with HSA. Fluorescence spectroscopy analysis revealed that the partial changes in the tertiary structure of the HSA resulted from the interaction between the aromatic compounds with the Al_2O_3 NPs. However, CD spectroscopy showed that the Al_2O_3 NPs did not affect the secondary structure of HSA. Also, based on docking

studies (Table 2), it was revealed that electrostatic forces were dominant in the interaction of HSA with different types of Al_2O_3 nano-clusters. Furthermore, based on the specific residues involved in the binding site of protein, it was determined that the cubic Al_2O_3 NPs had the highest tendency to interact with HSA due to the lowest energy barrier. In this regard, Ansari et al. (2018) showed that titanium oxide (TiO_2) NPs have no effect on the secondary structure of the protein, while similar to our findings, these NPs can affect the tertiary structure of HSA. It was also determined that the use of cerium oxide (CeO_2) NPs (Roudbaneh et al., 2019) and copper oxide (CuO) NPs (Konar et al., 2017) provided no substantial effect on protein structure. However, Treuel et al. (2010) and Capomaccio et al. (2015) exposed that gold and silver NPs stimulated substantial interactions with HSA along with considerable changes in the tertiary structure of adsorbed protein. Also, it was shown that Al_2O_3 NPs can induce some substantial conformational changes on the bovine serum albumin (BSA) (Rajeshwari et al., 2014) and hemoglobin (Hb) (Kahbasi et al., 2019). This difference between these reports and our data is due to the route selected for synthesis of Al_2O_3 NPs, the pH of the medium, the kind of target proteins, and experimental set up.

Taken together, the results of this study and other reports indicate that the secondary structure of the protein is preserved in the presence of metal oxide NPs, which may indicate that the protein denaturation is done in a reversible manner in the presence of NPs.

The cytotoxic effects of Al_2O_3 NPs show the dose-dependent inhibitory effects on cell growth of K562 cells as exhibited in the Fig. 5, whereas, Al_2O_3 NPs did not induce a significant effect on the lymphocyte viability after 24 hrs. Although, the interaction of Al_2O_3 NPs with osteoblasts and mammalian cells had no significant effect on their viability similar to lymphocyte cells (Radziun et al., 2011, Tripathi et al., 2013), contrary to our results, Sliwinska et al. (2015) revealed that Al_2O_3 NPs significantly reduced cell growth and the lymphocyte viability. The most important reason for the effect of Al_2O_3 NPs on lymphocyte cells could be the higher concentration of NPs and the incubation period. In point of fact, the effect of NPs on cancer cells derives from the type of cell, the geometry of NPs and the applied concentration of NPs. In this regard, inconsistent with our results, Chen et al. (2018) reported that Al_2O_3 NPs did not significantly decrease the viability of melanoma B16F10 tumor cells derived from mice. While, in an animal model it was found that the use of aluminum hydroxide [Al(OH)$_3$] NPs reduced the activity of melanoma cells (Lerner et al., 2018). In addition, Al_2O_3-dopt zinc oxide (ZnO) NPs were able to increase non-autophagic cell death of lung cancer cells in addition to decreasing the viability of A549 and CL1-5 cells through inhibiting expression of LC3 II gene (Bai et al., 2017). Recently, Subramaniam et al. (2019) described that Al_2O_3 NPs based on interacting with membrane lipids and stopping the critical activities of colon cancer cell membrane, in addition to reducing cancer cell growth by enhancing ROS-based apoptosis, prevented the morphological changes of cancer cells for metastatic activity. Similar to this report, our results confirmed that the Al_2O_3 NPs caused apoptosis induction in K562 cells via the internal pathway by up-regulating the Bax/ Bcl-2 mRNA ratio. Also, the high level of DCF intensity in the presence of Al_2O_3 NPs (Fig. 6A) indicated that apop-
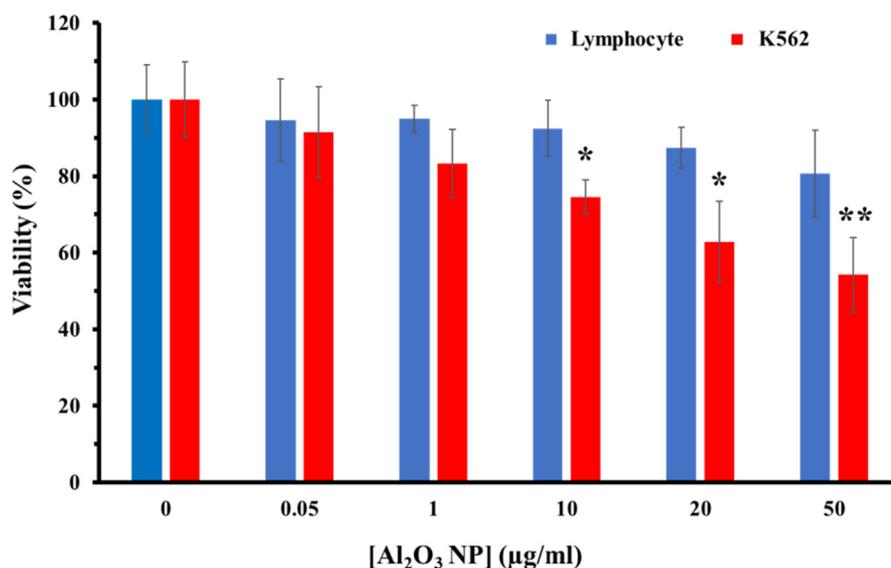
Fig. 5 Viability assay of K562 and lymphocyte cells in the presence of different concentrations (0.05–50 μg/ml) of Al_2O_3 NPs. *P < 0.5 and **P < 0.01 relative to negative untreated cells.
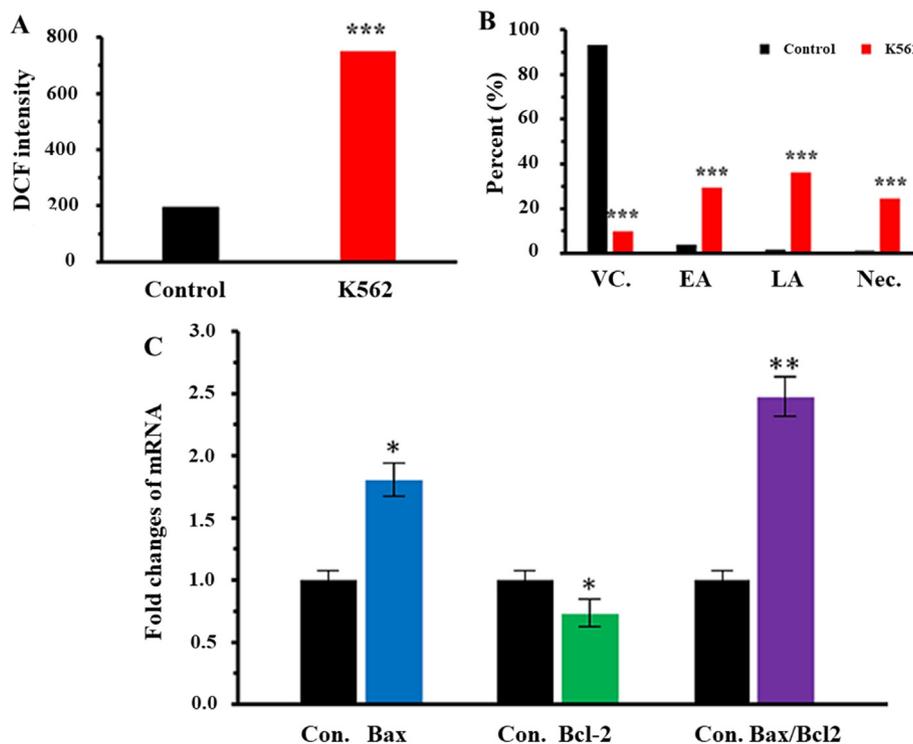
Fig. 6 **(A)** ROS assay of K562 cells either alone or incubated with highest concentration (50 μg/ml) of Al_2O_3 NPs for 24 hrs. **(B)** Annexin-V/PI assay of K562 cells either alone or incubated with highest concentration (50 μg/ml) of Al_2O_3 NPs for 24 hrs. **(C)** qPCR analysis of K562 cells incubated with highest concentration (50 μg/ml) of Al_2O_3 NPs for 24 hrs. *P < 0.5, **P < 0.01, and ***P < 0.001 relative to negative control cells. **Abbreviations:** Con.: control; VC.: viable cells; EA: early apoptosis; LA: late apoptosis; Nec: necrosis.

totic cell death induced by an increase in intracellular ROS level. Thus, despite the uncertainties in the mechanism of Al_2O_3 NPs toxicity to reduce cancer cell growth, this study emphasizes that Al_2O_3 NPs based on a concentration-dependent manner can be effective in controlling and reducing cancer cell proliferation in pre-clinical activities.

Regarding the antibacterial behavior of NPs, consistent with the results of Jwad et al. (2019) this report revealed that Al_2O_3 NPs triggered different inhibitory effects against both Gram-positive and Gram-negative bacteria in a concentration-dependent manner. The difference in response to the presence of Al_2O_3 NPs is related to the cell wall struc-
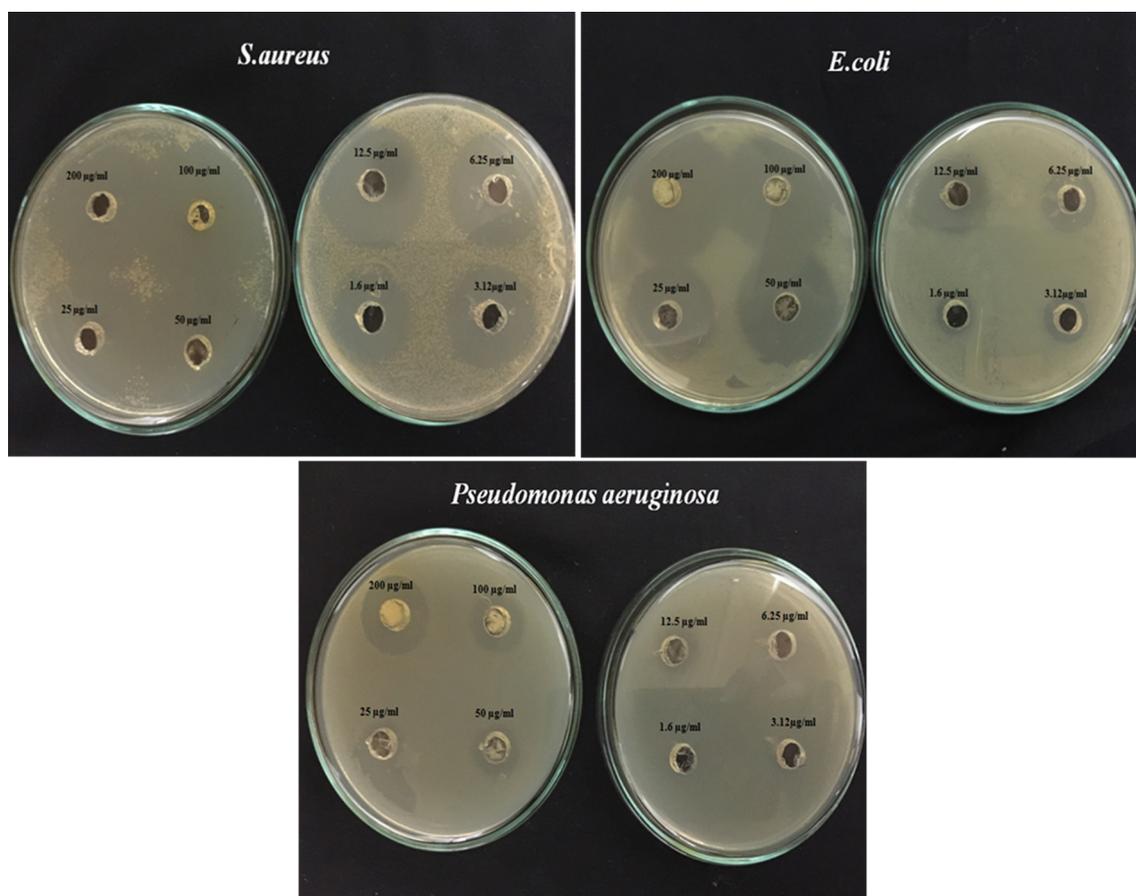
Fig. 7   Visible zone produced by varying concentrations (200–3.12 μg/ml) of Al$_2$O$_3$ NPs against *S. aureus*, *E. coli* and *P. aeruginosa*.

tures and the concentration of NPs accumulated in the bacteria. Because Gram-negative bacteria lack lipopolysaccharides in the cell wall, they are more resistant to lipophilic substances (Ansari et al., 2014). Moreover, Al ions, which can stimulate Fenton reactions and lead to elevation of ROS production as the concentration of Al$_2$O$_3$ NPs increases (Khatri et al., 2018). Therefore, Al$_2$O$_3$ NPs like other metal oxides, play an important role in inhibiting bacterial growth through oxidative stress, cell walls deformation and damage to the vital organelles, preventing enzyme activities, and DNA deformation (Ansari et al., 2014, Raghunath and Perumal, 2017). In this regard, Sadiq et al. (2011) and Bala et al. (2011) using Al$_2$O$_3$ NPs and Al$_2$O$_3$-silver nano-composite, respectively, showed high antipathogenic effect on microalgae isolated from aquatic environment, *E. coli*, and *P. aeruginosa* based on changes in cell wall of bacteria. In the following, Kandalkar et al. (2017) and Saxena and Pandey (2019) by applying antipathogenic activity of Al$_2$O$_3$ NPs, described that the NPs can inhibit the bacterial growth by interacting with the cell wall and increasing cytoplasmic leakage. Several studies have been carried out to promote the antibacterial activity of metal oxide NPs, which generally rely on the concentration and surface-to-volume ratio of metal oxide NPs (Sliwinska et al., 2015, Niño-Martínez et al., 2019, Sharifi et al., 2019b). For instance, similar to our work, Roudbaneh et al. (2019), Dadi et al. (2019), Abdolmajid et al. (2019), and Anbouhi et al. (2019) explained that an increase in the concentration of CeO$_2$ NPs, CuO NPs, TiO$_2$ NPs, and zero valent iron NPs, respectively

reduces the activity of *E. coli*, *P. aeruginosa* and *S. aureus*. Moreover, Zakharova et al. (2019) reported that the ZnO NPs show an antibacterial activity against *E. coli* which is heavily dependent on NP size, dispersion media and incubation time. Finally, this survey and the reports cited above show that Al$_2$O$_3$ NPs, similar to some other metal oxide NPs can exhibit outstanding antipathogenic activities.

5. Conclusion

This study demonstrated that the synthesized Al$_2$O$_3$ NPs could bind to HSA and quenches the fluorescence signals of the protein at room temperatures. Also, ANS and acrylamide fluorescence spectroscopy study revealed that Al$_2$O$_3$ NPs can induce some partial unfolding of HSA molecules in the vicinity of aromatic residues. Far-UV CD analysis depicted that Al$_2$O$_3$ NPs induced no significant changes in the secondary structural of HSA even at high concentrations. Theoretical methodology also demonstrated that spontaneous exothermic reactions occur between HSA and Al$_2$O$_3$ nano-clusters. Additionally, the cellular assays demonstrated that Al$_2$O$_3$ NPs can be considered as a potential antiproliferative agent and could stimulate these effects through ROS-dependent apoptosis pathways. Moreover, the antibacterial activity demonstrated that the Al$_2$O$_3$NPs provided outstanding antipathogenic activity against both Gram-negative and Gram-positive foodborne pathogens. Exploring the mechanisms by which NPs stimulate the anti-

cancer and antibacterial effects is a part of an approach to treat human tumors and bacterial infections; therefore, investigations concerning the mechanisms of the anticancer and antipathogenic impacts of the NPs on different targets merit further detailed studies *in vitro* and *in vivo*.

Declaration of Competing Interest

The authors declare that they have no known competing financial interests or personal relationships that could have appeared to influence the work reported in this paper.

Acknowledgement

References

Abbasi, M., Dorranian, D., 2015 Mar 1. Effect of laser fluence on the characteristics of Al nanoparticles produced by laser ablation in deionized water. Opt. Spectrosc. 118 (3), 472–481.

Abdolmajid, E., Kharazi, H., Chalaki, M., Khojasteh, M., Haghighat, S., Attar, F., Nemati, F., Falahati, M., 2019. Titanium oxide nanoparticles fabrication, hemoglobin interaction, white blood cells cytotoxicity, and antibacterial studies. J. Biomol. Struct. Dyn. 37, 3007–3017.

Aghili, Z., Taheri, S., Zeinabad, H.A., Pishkar, L., Saboury, A.A., Rahimi, A., Falahati, M., 2016. Investigating the interaction of Fe nanoparticles with lysozyme by biophysical and molecular docking studies. PLoS ONE 11, e0164878.

Anbouhi, T.S., Esfidvajani, E.M., Nemati, F., Haghighat, S., Sari, S., Attar, F., Pakaghideh, A., Sohrabi, M.J., Mousavi, S.E., Falahati, M., 2019. albumin binding, anticancer and antibacterial properties of synthesized zero valent iron nanoparticles. Int. J. Nanomed. 14, 243.

Ansari, A., Sachar, S., Garje, S.S., 2018. Synthesis of bare and surface modified TiO 2 nanoparticles via a single source precursor and insights into their interactions with serum albumin. New J. Chem. 42, 13358–13366.

Ansari, M., Khan, H., Khan, A., Cameotra, S.S., Saquib, Q., Musarrat, J., 2014. Interaction of A l2 O 3 nanoparticles with E scherichia coli and their cell envelope biomolecules. J. Appl. Microbiol. 116, 772–783.

Areerachakul, N., Sakulkhaemaruethai, S., Johir, M., Kandasamy, J., Vigneswaran, S., 2019. Photocatalytic degradation of organic pollutants from wastewater using aluminium doped titanium dioxide. J. Water Process Eng. 27, 177–184.

Ariga, K., Ji, Q., Nakanishi, W., Hill, J.P., Aono, M., 2015. Nanoarchitectonics: a new materials horizon for nanotechnology. Mater. Horiz. 2, 406–413.

Bai, K.-J., Chuang, K.-J., Ma, C.-M., Chang, T.-Y., Chuang, H.-C., 2017. Human lung adenocarcinoma cells with an EGFR mutation are sensitive to non-autophagic cell death induced by zinc oxide and aluminium-doped zinc oxide nanoparticles. J. Toxicol. Sci. 42, 437–444.

Bala, T., Armstrong, G., Laffir, F., Thornton, R., 2011. Titania–silver and alumina–silver composite nanoparticles: novel, versatile synthesis, reaction mechanism and potential antimicrobial application. J. Colloid Interface Sci. 356, 395–403.

Behzadi, E., Sarsharzadeh, R., Nouri, M., Attar, F., Akhtari, K., Shahpasand, K., Falahati, M., 2019. Albumin binding and anticancer effect of magnesium oxide nanoparticles. Int. J. Nanomed. 14, 257.

Bray, F., Ferlay, J., Soerjomataram, I., Siegel, R.L., Torre, L.A., Jemal, A., 2018. Global cancer statistics 2018: GLOBOCAN estimates of incidence and mortality worldwide for 36 cancers in 185 countries. CA Cancer J. Clin. 68, 394–424.

Capomaccio, R., Jimenez, I.O., Colpo, P., Gilliland, D., Ceccone, G., Rossi, F., Calzolai, L., 2015. Determination of the structure and morphology of gold nanoparticle–HSA protein complexes. Nanoscale 7, 17653–17657.

Chen, W., Qin, M., Chen, X., Wang, Q., Zhang, Z., Sun, X., 2018. Combining photothermal therapy and immunotherapy against melanoma by polydopamine-coated Al(2)O(3) nanoparticles. Theranostics 8, 2229–2241.

Chibber, S., Ahmad, I., 2016. Molecular docking, a tool to determine interaction of CuO and TiO2 nanoparticles with human serum albumin. Biochem. Biophys. Rep. 6, 63–67.

Dabagh, S., Chaudhary, K., Haris, S.A., Haider, Z., Ali, J., 2018. Aluminium Substituted Ferrite Nanoparticles with Enhanced Antibacterial Activity. J. Comput. Theor. Nanosci. 15, 1052–1058.

Dadi, R., Azouani, R., Traore, M., Mielcarek, C., Kanaev, A., 2019. Antibacterial activity of ZnO and CuO nanoparticles against gram positive and gram negative strains. Mater. Sci. Eng. C 104, 109968.

Esfandfar, P., Falahati, M., Saboury, A., 2016. Spectroscopic studies of interaction between CuO nanoparticles and bovine serum albumin. J. Biomol. Struct. Dyn. 34, 1962–1968.

Falahati, M., Attar, F., Sharifi, M., Haertlé, T., Berret, J.-F., Khan, R. H., and Saboury, A. A., 2019a. A health concern regarding the protein corona, aggregation and disaggregation. Biochimica et Biophysica Acta (BBA)-General Subjects.

Falahati, M., Ghoraeian, P.G., Haji Hosseinali, S., 2019b. Albumin binding and cytotoxicity assay of nickel oxide nanoparticles against primary hippocampal neural cells. J. Nanoanal.

Falahati, M., Saboury, A.A., Shafiee, A., Sorkhabadi, S.M.R., Kachooei, E., Ma'Mani, L., Haertlé, T., 2012. Highly efficient immobilization of beta-lactoglobulin in functionalized mesoporous nanoparticles: A simple and useful approach for enhancement of protein stability. Biophys. Chem. 165, 13–20.

Fu, X., Ren, F.-F., Sun, S., Tian, Y., Wu, Y., Lou, P., Du, Q.G., 2019. High-sensitivity nanostructured aluminium ultrathin film sensors with spectral response from ultraviolet to near-infrared. Phys. Scr. 94, 055504.

Gilan, S.S.T., Rayat, D.Y., Mustafa, T.A., Aziz, F.M., Shahpasand, K., Akhtari, K., Salihi, A., Abou-Zied, O.K., Falahati, M., 2019. α-synuclein interaction with zero-valent iron nanoparticles accelerates structural rearrangement into amyloid-susceptible structure with increased cytotoxic tendency. Int. J. Nanomed. 14, 4637.

Hajsalimi, G., Taheri, S., Shahi, F., Attar, F., Ahmadi, H., Falahati, M., 2018. Interaction of iron nanoparticles with nervous system: an in vitro study. J. Biomol. Struct. Dyn. 36, 928–937.

Hartshorn, C.M., Bradbury, M.S., Lanza, G.M., Nel, A.E., Rao, J., Wang, A.Z., Wiesner, U.B., Yang, L., Grodzinski, P., 2017. Nanotechnology strategies to advance outcomes in clinical cancer care. ACS Nano 12, 24–43.

He, H., Markoutsa, E., Li, J., Xu, P., 2018. Repurposing disulfiram for cancer therapy via targeted nanotechnology through enhanced tumor mass penetration and disassembly. Acta Biomater. 68, 113–124.

Huang, P., Wang, X., Liang, X., Yang, J., Zhang, C., Kong, D., Wang, W., 2018. Nano-, micro-, and macroscale drug delivery systems for cancer immunotherapy. Acta Biomater.

Jurj, A., Braicu, C., Pop, L.-A., Tomuleasa, C., Gherman, C.D., Berindan-Neagoe, I., 2017. The new era of nanotechnology, an

alternative to change cancer treatment. Drug Des. Develop. Therapy 11, 2871.

Iqbal, M., Khan, S.A., Ivanov, D.S., Ganeev, R.A., Kim, V.V., Boltaev, G.S., Sapaev, I., Abbasi, N.A., Shaju, S., Garcia, M.E., Rethfeld, B., 2020 May. The mechanism of laser-assisted generation of aluminum nanoparticles, their wettability and nonlinearity properties. Appl. Surf. Sci. 25, 146702.

Ismail, R.A., Zaidan, S.A., Kadhim, R.M., 2017 Oct 1. Preparation and characterization of aluminum oxide nanoparticles by laser ablation in liquid as passivating and anti-reflection coating for silicon photodiodes. Applied Nanoscience. 7 (7), 477–487.

Jwad, K.H., Saleh, T.H., Abd-Alhamza, B., 2019. Preparation of Aluminum Oxide Nanoparticles by Laser Ablation and a Study of Their Applications as Antibacterial and Wounds Healing Agent. Nano Biomed. Eng 11, 313–319.

Kahbasi, S., Samadbin, M., Attar, F., Heshmati, M., Danaei, D., Rasti, B., Salihi, A., Nanakali, N.M.Q., Aziz, F.M., Akhtari, K., 2019. The effect of aluminum oxide on red blood cell integrity and hemoglobin structure at nanoscale. Int. J. Biol. Macromol. 138, 800–809.

Kandalkar, P., Gadhikar, Y., Waghuley, S., 2017. Synthesis of Aluminum Doped Zinc Oxide Nanoparticles for Antibacterial Activity. Int. J. Res. Biosci. Agri. Technol. 7, 72–76.

Khatri, J., Nidheesh, P., Singh, T.A., Kumar, M.S., 2018. Advanced oxidation processes based on zero-valent aluminium for treating textile wastewater. Chem. Eng. J. 348, 67–73.

Konar, S., Sen, S., Pathak, A., 2017. Morphological Effects of CuO Nanostructures on Fibrillation of Human Serum Albumin. J. Phys. Chem. B 121, 11437–11448.

Kumar, A., Prasad, M., Janyani, V., Yadav, R., 2019. Fabrication and Simulation of Piezoelectric Aluminium Nitride Based Micro Electro Mechanical System Acoustic Sensor. J. Nanoelectron. Optoelectron. 14, 1267–1274.

Kusper, M., Guisbiers, G., 2018. Synthesis of aluminum oxide nanoparticles by laser ablation in liquids. MRS Adv. 3 (64), 3899–3903.

Lam, J., Amans, D., Chaput, F., Diouf, M., Ledoux, G., Mary, N., Masenelli-Varlot, K., Motto-Ros, V., Dujardin, C., 2014. γ-Al 2 O 3 nanoparticles synthesised by pulsed laser ablation in liquids: a plasma analysis. PCCP 16 (3), 963–973.

Lee, S., Ahn, A., Choi, M.Y., 2012. Direct observation of aluminium ions produced via pulsed laser ablation in liquid: A 'turn-on'fluorescence study. PCCP 14 (45), 15677–15681.

Lerner, M.I., Mikhaylov, G., Tsukanov, A.A., Lozhkomoev, A.S., Gutmanas, E., Gotman, I., Bratovs, A., Turk, V., Turk, B., Psakhye, S.G., Vasiljeva, O., 2018. Crumpled Aluminum Hydroxide Nanostructures as a Microenvironment Dysregulation Agent for Cancer Treatment. Nano Lett. 18, 5401–5410.

Liang, J., Azhar, U., Men, P., Chen, J., Liu, Y., He, J., Geng, B., 2019. Fluoropolymer/SiO2 encapsulated aluminum pigments for enhanced corrosion protection. Appl. Surf. Sci. 487, 1000–1007.

Mansouri, A., Mousavi, M., Attar, F., Saboury, A.A., Falahati, M., 2018. Interaction of manganese nanoparticle with cytochrome c: A multi-spectroscopic study. Int. J. Biol. Macromol. 106, 78–86.

Mintcheva, N., Yamaguchi, S., Kulinich, S.A., 2020 Jan. Hybrid TiO2-ZnO Nanomaterials Prepared Using Laser Ablation in Liquid. Materials 13 (3), 719.

Muzammil, S., Hayat, S., Fakhar-E-Alam, M., Aslam, B., Siddique, M., Nisar, M., Saqalein, M., Atif, M., Sarwar, A., Khurshid, A., 2018. Nanoantibiotics: Future nanotechnologies to combat antibiotic resistance. Front Biosci (Elite Ed) 10, 352–374.

Nikalje, A.P., 2015. Nanotechnology and its applications in medicine. Med. Chem. 5, 81–89.

Niño-Martínez, N., Salas Orozco, M.F., Martínez-Castañón, G.-A., Torres Méndez, F., Ruiz, F., 2019. Molecular Mechanisms of Bacterial Resistance to Metal and Metal Oxide Nanoparticles. Int. J. Mol. Sci. 20, 2808.

Radziun, E., Dudkiewicz Wilczynska, J., Ksiazek, I., Nowak, K., Anuszewska, E.L., Kunicki, A., Olszyna, A., Zabkowski, T., 2011. Assessment of the cytotoxicity of aluminium oxide nanoparticles on selected mammalian cells. Toxicol In Vitro 25, 1694–1700.

Raghunath, A., Perumal, E., 2017. Metal oxide nanoparticles as antimicrobial agents: a promise for the future. Int. J. Antimicrob. Agents 49, 137–152.

Rajeshwari, A., Pakrashi, S., Dalai, S., Iswarya, V., Chandrasekaran, N., Mukherjee, A., 2014. Spectroscopic studies on the interaction of bovine serum albumin with Al2O3 nanoparticles. J. Lumin. 145, 859–865.

Ramos, M.A.D.S., Da Silva, P.B., Sposito, L., De Toledo, L.G., Bonifacio, B.V., Rodero, C.F., Dos Santos, K.C., Chorilli, M., Bauab, T.M., 2018. Nanotechnology-based drug delivery systems for control of microbial biofilms: a review. Int. J. Nanomed. 13, 1179.

Riahi, A., Khamlich, S., Balghouthi, M., Khamliche, T., Doyle, T.B., Dimassi, W., Guizani, A., Maaza, M., 2020 Apr. Study of thermal conductivity of synthesized Al2O3-water nanofluid by pulsed laser ablation in liquid. J. Mol. Liq. 15, (304) 112694.

Piriyawong, V., Thongpool, V., Asanithi, P., Limsuwan, P., 2012. Preparation and characterization of alumina nanoparticles in deionized water using laser ablation technique. J. Nanomater. 1, 1–10.

Roudbaneh, S.Z.K., Kahbasi, S., Sohrabi, M.J., Hasan, A., Salihi, A., Mirzaie, A., Niyazmand, A., Nanakali, N.M.Q., Shekha, M.S., Aziz, F.M., 2019. Albumin binding, antioxidant and antibacterial effects of cerium oxide nanoparticles. J. Mol. Liq. 296, 111839.

Sabziparvar, N., Saeedi, Y., Nouri, M., Najafi Bozorgi, A.S., Alizadeh, E., Attar, F., Akhtari, K., Mousavi, S.E., Falahati, M., 2018. Investigating the Interaction of Silicon Dioxide Nanoparticles with Human Hemoglobin and Lymphocyte Cells by Biophysical, Computational, and Cellular Studies. J. Phys. Chem. B 122, 4278–4288.

Sadiq, I.M., Pakrashi, S., Chandrasekaran, N., Mukherjee, A., 2011. Studies on toxicity of aluminum oxide (Al2O3) nanoparticles to microalgae species: Scenedesmus sp. and Chlorella sp. J. Nanopart. Res. 13, 3287–3299.

Saxena, V., Pandey, L.M., 2019. Synthesis, characterization and antibacterial activity of aluminum doped zinc oxide. Mater. Today. Proc. 18, 1388–1400.

Shankar, P., Ishak, M.H., Padarti, J.K., Mintcheva, N., Iwamori, S., Gurbatov, S.O., Lee, J.H., Kulinich, S.A., 2020 Nov. ZnO@ graphene oxide core@ shell nanoparticles prepared via one-pot approach based on laser ablation in water. Appl. Surf. Sci. 30, (531) 147365.

Sharifi, M., Attar, F., Saboury, A.A., Akhtari, K., Hooshmand, N., Hasan, A., El-Sayed, M., Falahati, M., 2019a. Plasmonic gold nanoparticles: Optical manipulation, imaging, drug delivery and therapy. J. Control. Release 311–312, 170–189.

Sharifi, M., Hosseinali, S.H., Saboury, A.A., Szegezdi, E., Falahati, M., 2019b. Involvement of planned cell death of necroptosis in cancer treatment by nanomaterials: Recent advances and future perspectives. J Control Release 299, 121–137.

Sharifi, M., Rezayat, S.M., Akhtari, K., Hasan, A., Falahati, M., 2019c. Fabrication and evaluation of anti-cancer efficacy of lactoferrin-coated maghemite and magnetite nanoparticles. J. Biomol. Struct. Dyn., 1–10

Sliwinska, A., Kwiatkowski, D., Czarny, P., Milczarek, J., Toma, M., Korycinska, A., Szemraj, J., Sliwinski, T., 2015. Genotoxicity and cytotoxicity of ZnO and Al2O3 nanoparticles. Toxicol. Mech. Meth. 25, 176–183.

Subramaniam, V.D., Ramachandran, M., Marotta, F., Banerjee, A., Sun, X.F., Pathak, S., 2019. Comparative study on anti-proliferative potentials of zinc oxide and aluminium oxide nanoparticles in colon cancer cells. Acta bio-medica : Atenei Parmensis 90, 241–247.

Treuel, L., Malissek, M., Gebauer, J.S., Zellner, R., 2010. The influence of surface composition of nanoparticles on their interactions with serum albumin. ChemPhysChem 11, 3093–3099.

Tripathi, G., Gough, J.E., Dinda, A., Basu, B., 2013. In vitro cytotoxicity and in vivo osseointergration properties of compression-molded HDPE-HA-Al2O3 hybrid biocomposites. J. Biomed. Mater. Res. A 101, 1539–1549.

Usman, M.S., Hussein, M.Z., Kura, A.U., Fakurazi, S., Masarudin, M.J., Saad, F.F.A., 2020. Chlorogenic acid intercalated Gadolinium–Zinc/Aluminium layered double hydroxide and gold nanohybrid for MR imaging and drug delivery. Mater. Chem. Phys. 240, 122232.

Van Duijkeren, E., Schink, A.-K., Roberts, M. C., Wang, Y., and Schwarz, S., 2018. Mechanisms of bacterial resistance to antimicrobial agents. Microbiology spectrum 6.

Yang, R., Xu, J., Xu, L., Sun, X., Chen, Q., Zhao, Y., Peng, R., Liu, Z., 2018. Cancer cell membrane-coated adjuvant nanoparticles with mannose modification for effective anticancer vaccination. ACS Nano 12, 5121–5129.

Zakharova, O., Kolesnikov, E., Vishnyakova, E., Strekalova, N., Gusev, A., 2019. Antibacterial activity of ZnO nanoparticles: dependence on particle size, dispersion media and storage time. IOP Conference Series Earth Environ. Sci. 226, 012062.

Zeinabad, H.A., Kachooei, E., Saboury, A.A., Kostova, I., Attar, F., Vaezzadeh, M., Falahati, M., 2016. Thermodynamic and conformational changes of protein toward interaction with nanoparticles: a spectroscopic overview. RSC Adv. 6, 105903–105919.

Zeng, H., Du, X.W., Singh, S.C., Kulinich, S.A., Yang, S., He, J., Cai, W., 2012. Nanomaterials via laser ablation/irradiation in liquid: a review. Adv. Funct. Mater. 22 (7), 1333–1353.